Journal of Solid State Chemistry 182 (2009) 356–363

Contents lists available at ScienceDirect

Journal of Solid State Chemistry

journal homepage: www.elsevier.com/locate/jssc

Synthesis, crystal structure and magnetic properties of the $Sr_2Al_{0.78}Mn_{1.22}O_{5.2}$ anion-deficient layered perovskite

Hans D'Hondt [a,*], Joke Hadermann [a], Artem M. Abakumov [a,b], Anna S. Kalyuzhnaya [b], Marina G. Rozova [b], Alexander A. Tsirlin [b], Ramesh Nath [c], Haiyan Tan [a], Jo Verbeeck [a], Evgeny V. Antipov [b], Gustaaf Van Tendeloo [a]

[a] EMAT, University of Antwerp, Groenenborgerlaan 171, B-2020 Antwerp, Belgium
[b] Department of Chemistry, Moscow State University, 119991 Moscow, Russia
[c] Max Planck Institute for Chemical Physics of Solids, 01187 Dresden, Germany

ARTICLE INFO

Article history:
Received 30 July 2008
Received in revised form
22 October 2008
Accepted 2 November 2008
Available online 13 November 2008

Keywords:
Oxides
Crystal structure
Transmission electron microscopy
Electron diffraction
X-ray diffraction
Perovskite
Brownmillerite
Local structure
Oxygen deficient
EELS

ABSTRACT

A new layered perovskite $Sr_2Al_{0.78}Mn_{1.22}O_{5.2}$ has been synthesized by solid state reaction in a sealed evacuated silica tube. The crystal structure has been determined using electron diffraction, high-resolution electron microscopy, and high-angle annular dark field imaging and refined from X-ray powder diffraction data (space group *P4/mmm*, $a = 3.89023(5)$ Å, $c = 7.8034(1)$ Å, $R_I = 0.023$, $R_P = 0.015$). The structure is characterized by an alternation of MnO_2 and $(Al_{0.78}Mn_{0.22})O_{1.2}$ layers. Oxygen atoms and vacancies, as well as the Al and Mn atoms in the $(Al_{0.78}Mn_{0.22})O_{1.2}$ layers are disordered. The local atomic arrangement in these layers is suggested to consist of short fragments of brownmillerite-type tetrahedral chains of corner-sharing AlO_4 tetrahedra interrupted by MnO_6 octahedra, at which the chain fragments rotate over 90°. This results in an averaged tetragonal symmetry. This is confirmed by the valence state of Mn measured by EELS. The relationship between the $Sr_2Al_{0.78}Mn_{1.22}O_{5.2}$ tetragonal perovskite and the parent $Sr_2Al_{1.07}Mn_{0.93}O_5$ brownmillerite is discussed. Magnetic susceptibility measurements indicate spin glass behavior of $Sr_2Al_{0.78}Mn_{1.22}O_{5.2}$. The lack of long-range magnetic ordering contrasts with Mn-containing brownmillerites and is likely caused by the frustration of interlayer interactions due to presence of the Mn atoms in the $(Al_{0.78}Mn_{0.22})O_{1.2}$ layers.

1. Introduction

The A_2BMnO_5 (A = Ca, Sr, B = Al, Ga) brownmillerites demonstrate a rich crystal chemistry and a delicate interplay between different crystal structures with variable oxygen content and electronic properties, such as colossal magnetoresistance [1–10]. Treated at oxidizing conditions, these brownmillerites can acquire an excess of oxygen up to $A_2BMnO_{5.5}$. For Ca_2BMnO_5 (B = Al, Ga), the oxidation leads to a second member of the brownmillerite-based homologous series $Ca_4B_{tet}B_{oct}(Mn_{oct})_2O_{11}$ (the subscripts $_{tet}$ and $_{oct}$ stand for the cations in the tetrahedrally and octahedrally coordinated positions, respectively), with the OOOTOOOT polyhedral sequence along the stacking axis of the octahedral (O) and tetrahedral (T) layers [1,11]. In contrast to that, oxidation and fluorination of Sr_2GaMnO_5 results in the insertion of extra anions into all (GaO) tetrahedral layers. This structural modification is accompanied by a decrease of the orthorhombic distortion up to the formation of tetragonal layered perovskites with $a \approx a_{per}$, $c \approx 2a_{per}$ (a_{per}—a parameter of the perovskite subcell) [2,12–16]. In all cases, the oxidation occurs at relatively soft conditions preserving the layered arrangement of the B and Mn cations in the initial brownmillerite phase. Thus, the synthesis of such layered perovskites comprises two major steps. The first one is the preparation of the anion-deficient brownmillerite phase where the cation ordering at the B-sites is promoted by simultaneous ordering of oxygen atoms and vacancies. In the second step, vacant anion positions are filled by extra anions.

In the present contribution we report on the preparation, structure and magnetic properties of the $Sr_2Al_{0.78}Mn_{1.22}O_{5.2}$ tetragonal perovskite with a layered ordering of the Al and Mn cations even in the absence of long range oxygen-vacancy ordering within the anion-deficient $BO_{1.2}$ layers. The relationship between this tetragonal perovskite structure and the parent $Sr_2Al_{1.07}Mn_{0.93}O_5$ brownmillerite is discussed.

2. Experimental

The $Sr_2Al_{1-x}Mn_{1+x}O_{5+\delta}$ samples were prepared from Mn_2O_3, MnO_2, Al_2O_3 ("Reakhim", "pure for analysis" purity grade), and SrO. SrO was obtained by thermal decomposition of

* Corresponding author. Fax: +32 32 653 257.
E-mail address: hans.dhondt@ua.ac.be (H. D'Hondt).

0022-4596/$ - see front matter © 2008 Elsevier Inc. All rights reserved.
doi:10.1016/j.jssc.2008.11.002

$SrCO_3$ (“Reakhim”, “pure for analysis” purity grade) at 1050 °C for 36 h in a dynamic vacuum of 10^{-4} mbar. The overall oxygen content of the samples was varied by changing the Mn_2O_3/MnO_2 ratio. The appropriate amounts of the oxides were mixed in an Ar-filled glove box, pressed into pellets, placed in alumina crucibles and sealed into evacuated silica tubes with a volume of ~10 cm^3. The samples were subsequently annealed at 1000 °C for 50 h and at 1100 °C for 48 h with an intermediate regrinding.

X-ray powder diffraction (XRPD) data for phase analysis and cell parameter determination were collected on a Huber G670 Guinier diffractometer (Cu$K\alpha_1$ radiation, curved Ge monochromator, transmission mode, image plate). XRPD data for crystal structure refinement were collected on a STADI-P diffractometer (Cu$K\alpha_1$-radiation, curved Ge monochromator, transmission mode, linear PSD). The JANA2000 program package was used for the Rietveld refinement of the crystal structure [17].

The samples for electron microscopy investigation were prepared by crushing the powder sample in ethanol and depositing it on a holey carbon grid. Electron diffraction (ED) studies were performed using a Philips CM20 microscope, and for high-resolution transmission electron microscopy (HRTEM) a JEOL 4000EX microscope was used. Energy dispersive X-ray (EDX) spectra were obtained on the Philips CM20 microscope with an Oxford INCA system. The theoretical HRTEM images were calculated by means of the Jems software. High-angle annular dark field (HAADF) images were acquired using a JEOL 3000F scanning transmission electron microscope (STEM). EELS data were acquired using a Gatan GIF200 system on a Philips CM30 microscope with an acceleration voltage of 300 kV and an energy resolution of 0.8 eV. All spectra were recorded in diffraction mode with a collection angle of 4.01 mrad and a convergence angle of 1.0 mrad. EELSMODEL [18–21] program package was used to extract the excitation edge fine structures of the recorded spectra.

The magnetic susceptibility was measured using a Quantum Design MPMS SQUID magnetometer in the temperature range 2–380 K in the applied field of 0.5 T. Both field cooling (FC) and zero field cooling (ZFC) regimes were studied. The magnetization (M vs. H) curve was recorded at 2 K after cooling the sample in zero field.

3. Results

3.1. Preliminary characterization

The perovskite-like phase dominates in the samples with the $Sr_2Al_{1-x}Mn_{1+x}O_5$ ($x = 0.1,0.2,0.3$) bulk compositions. On the XRPD patterns, the reflections of this phase can be indexed on a tetragonal unit cell with cell parameters $a \approx a_{per}$, $c \approx 2a_{per}$. The parameters decrease monotonically with increasing x: $a = 3.9083(3)$ Å, $c = 7.8170(14)$ Å ($x = 0.1$); $a = 3.9026(3)$ Å, $c = 7.7994(13)$ Å ($x = 0.2$); $a = 3.8837(11)$ Å, $c = 7.7772(16)$ Å ($x = 0.3$). In the $x = 0.1$ sample, weak reflections with a relative intensity of 1–3% were observed indicating a minor admixture of the $Sr_2Al_{1.07}Mn_{0.93}O_5$ brownmillerite [8]. In all the samples, $Sr_{12}Al_{14}O_{33}$, $Sr_3Al_2O_6$ or $SrAl_2O_4$, and MnO admixtures were present (with maximal intensity of the admixture reflections of ~5%). The appearance of MnO in the reaction product indicates that the oxidation state of the Mn cations in the perovskite tetragonal phase is higher than +3 due to the partial disproportionation of Mn(III): 2Mn(III)→Mn(II)+Mn(IV). This assumption is supported by an estimate of the upper value of the partial oxygen pressure in the sealed silica tube at the synthesis temperature. The partial oxygen pressure cannot be higher than the equilibrium oxygen pressure above the MnO/Mn_3O_4 mixture at 1100 °C ($P(O_2) \approx 2.5 \times 10^{-6}$ atm). This reflects negligible loss of oxygen into the free volume of the silica tube and confirms that the appearance of MnO mainly occurs due to disproportionation.

In order to diminish the amount of admixture phases, samples with higher oxygen content were prepared. The best sample was obtained for the bulk composition $Sr_2Al_{0.7}Mn_{1.3}O_{5.13}$ ($V_{Mn} = +3.2$, 10 mol% of Mn_2O_3 was replaced by MnO_2 to achieve the nominal oxygen content) and contained only 2.2 wt% of MnO (determined from Rietveld refinement). Assuming that only the 2Mn(III)→Mn(II)+Mn(IV) disproportionation takes place, one can calculate the formal Mn valence in the perovskite phase from the amount of the MnO admixture as $V_{Mn} = +3.33$. This value is further confirmed by EELS measurements. Taking into account the cation composition, as determined by EDX analysis and later confirmed by Rietveld refinement, the chemical composition of the tetragonal phase can be written as $Sr_2Al_{0.78}Mn_{1.22}O_{5.2}$. A further increase of the oxygen content in the initial reaction mixture results in an increasing amount of admixtures of strontium aluminates and does not improve the quality of the samples.

3.2. Electron diffraction

A complete study of the reciprocal lattice was performed by taking ED patterns from different crystals of $Sr_2Al_{0.78}Mn_{1.22}O_{5.2}$ along different zones axes of different tilt series. All ED patterns can be indexed using a tetragonal unit cell with $a \approx a_{per}$ and $c \approx 2a_{per}$, in agreement with the results of the XRPD investigation. The ED patterns along the main zones of $Sr_2Al_{0.78}Mn_{1.22}O_{5.2}$ are shown in Fig. 1a, b, and d. All crystals of $Sr_2Al_{0.78}Mn_{1.22}O_{5.2}$ viewed along [100] demonstrate 90° rotation twinning. This explains the reflections observed at the positions 0, k+1/2, 0 (Fig. 1a). A schematic representation of the overlapping twin variants is drawn next to the experimental pattern (Fig. 1c). No systematic extinctions were detected suggesting the most symmetrical tetragonal space group $P4/mmm$. This space group and the cell parameters listed above are typical for tetragonal layered perovskites, such as the anion-excessive derivatives of the

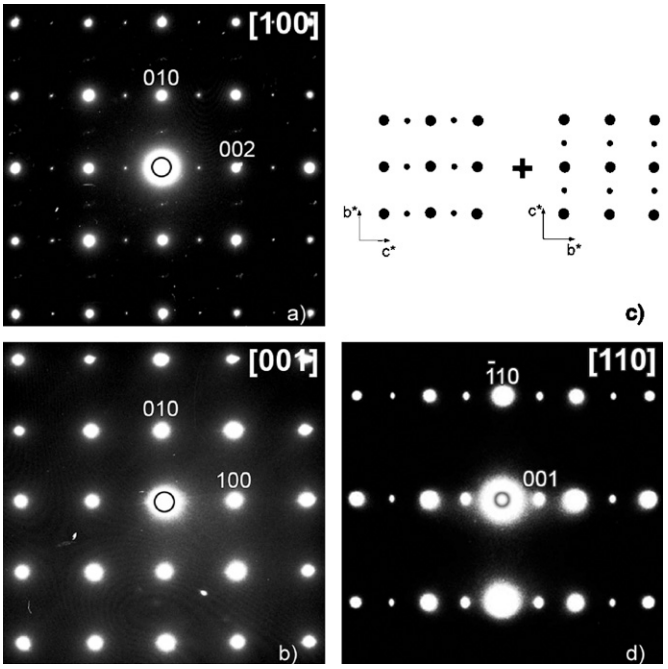

Fig. 1. Electron diffraction patterns of the main zones of $Sr_2Al_{0.78}Mn_{1.22}O_{5.2}$: (a) [100]; (b) [001]; (c) scheme of the twinning observed in the [100] pattern; and (d) [110].

brownmillerites $Sr_2MnGaO_{5.5}$ [12], $LaSrCuGaO_{5-x}F_{2x}$ [22], and $Sr_2MnGa(O,F)_6$ [13].

3.3. Rietveld refinement

The starting model of the $Sr_2Al_{0.78}Mn_{1.22}O_{5.2}$ structure for the Rietveld refinement was constructed in an assumption that the doubling of the perovskite unit cell parameter along the *c* axis is caused by a layered ordering of the Mn and Al cations. One could expect that deviations in the cation and oxygen stoichiometry of the $Sr_2Al_{0.78}Mn_{1.22}O_{5.2}$ phase (as compared to the ideal brownmillerite $A_2BB'O_5$) would cause a transformation of the $B'O$ tetrahedral layer with ordered anion vacancies into a disordered anion-deficient layer. In this layer, fragments of the brownmillerite tetrahedral chains are retained, being randomly oriented and terminating at the MnO_6 octahedra. These features should be reflected in disordered atomic displacements from the special positions of the *P*4/*mmm* space group.

In the starting model, the octahedral Mn layer was positioned at $z = 0$ and the mixed (Al, Mn) layer was located at $z = \frac{1}{2}$. In the $Sr_2Al_{1.07}Mn_{0.93}O_5$ brownmillerite, the cations in the tetrahedral layer are displaced from the ideal position mainly along the $\langle 110 \rangle$ perovskite direction [8]. Therefore, the Al atoms in the (Al, Mn) layer of $Sr_2Al_{0.78}Mn_{1.22}O_{5.2}$ were placed at the 4*k* (x,x,$\frac{1}{2}$) position instead of 1*b* (0,0,$\frac{1}{2}$). The Mn atoms in this layer were kept at the 1*b* position. The occupancy factors for these Al_1 and Mn_2 atoms were then refined at fixed $U_{iso} = 0.02$ Å^2. The refined Al/Mn ratio was found to be 0.78/0.22 (occupancy factors $g(Al_1) = 0.195(6)$ and $g(Mn_2) = 0.222(6)$). The oxygen atom O_3 located in the (Al, Mn) layer at the position ($\frac{1}{2}$,0,$\frac{1}{2}$) was refined with an abnormally large atomic displacement parameter (ADP) $U_{iso} = 0.188(3)$ Å^2. A displacement of the O_3 atom to the position ($\frac{1}{2}$,y,$\frac{1}{2}$) and refinement of its occupancy factor ($g(O_3) = 0.308(4)$) reduced the ADP to a more reasonable value (see Table 2). The chemical composition $Sr_2Al_{0.78}Mn_{1.22}O_{5.23}$ deduced from the Rietveld refinement is in good agreement with the results of the EDX analysis and the oxygen content calculated from the amount of the MnO admixture. For the final refinement, the occupancy factors of the Al_1, Mn_2, and O_3 positions were set to satisfy the $Sr_2Al_{0.78}Mn_{1.22}O_{5.2}$ composition, and the ADPs for all the atoms were refined in an isotropic approximation. Preferred orientation was taken into account using a March-Dollase formula. The refinement (with MnO as a second phase) resulted in reasonably low reliability factors $R_I = 0.023$, $R_P = 0.015$. The crystallographic data and atomic coordinates are summarized in Tables 1 and 2. The most relevant interatomic distances are listed in Table 3. Experimental, calculated, and difference XRPD profiles are shown in Fig. 2.

Table 1
Selected parameters from the Rietveld refinement for $Sr_2Al_{0.78}Mn_{1.22}O_{5.2}$.

Formula	$Sr_2Al_{0.78}Mn_{1.22}O_{5.2}$
Space group	*P*4/*mmm*
a (Å)	3.89023(5)
c (Å)	7.8034(1)
Cell volume (Å^3)	118.097(3)
Z	1
Calculated density (g/cm^3)	4.871
2θ range, step (°)	$10 \leqslant 2\theta \leqslant 100$; 0.01
Radiation, λ (Å)	1.5406
Preferred orientation parameter and axis	1.089(3), [001]
Number of refineable parameters	15
Number of reflections	54
R_I, R_P, R_{wP}	0.023, 0.015,0.021

Table 2
Atomic positions and thermal parameters for $Sr_2Al_{0.78}Mn_{1.22}O_{5.2}$.

Atom	Position	Occupancy	*x*/*a*	*y*/*a*	*z*/*c*	U_{iso} (Å^2)
Sr_1	2*h*	1	1/2	1/2	0.2315(1)	0.0158(2)
Mn_1	1*a*	1	0	0	0	0.021(1)
Al_1	4*k*	0.195Al	0.030(8)	0.030(8)	1/2	0.020(3)
Mn_2	1*b*	0.222Mn	0	0	1/2	0.020(3)
O_1	2*f*	1	1/2	0	0	0.019(2)
O_2	2*g*	1	0	0	0.2767(7)	0.043(3)
O_3	4*o*	0.3O	1/2	0.139(4)	1/2	0.043(5)

Table 3
Main interatomic distances for $Sr_2Al_{0.78}Mn_{1.22}O_{5.2}$ (Å).

Sr_1–O_1	2.6546(7) × 4	Al_1–O_2	1.751(6) × 2
Sr_1–O_2	2.7733(7) × 4	Al_1–O_3	1.87(3) × 2
Sr_1–O_3	2.522(8) × 4	Al_1–O_3	1.94(3) × 2
Sr_1–O_3	3.251(11) × 4	Al_1–O_3	2.11(3) × 2
Mn_1–O_1	1.9451(1) × 4	Al_1–O_3	2.17(3) × 2
Mn_1–O_2	2.159(5) × 2	Mn_2–O_2	1.743(5) × 2
		Mn_2–O_3	2.019(4) × 8

The supplementary material has been sent to the Fachinformationszentrum Karlsruhe, Abt. PROKA, 76344 Eggenstein-Leopoldshafen, Germany, as supplementary material no. SUP 419329 and can be obtained by contacting the FIZ (quoting the article details and the corresponding SUP number).

The crystal structure of $Sr_2Al_{0.78}Mn_{1.22}O_{5.2}$ is shown in Fig. 3. The Mn_1 atoms adopt a distorted octahedral environment with four short equatorial Mn_1–O_1 distances of 1.9451(1) Å and two longer apical Mn_1–O_2 distances of 2.159(5) Å. The bond valence sum calculated for the Mn_1 cation in assumption of $R_0 = 1.76$ (taken as R_0 for Mn^{+3}) was found to be 3.1 in acceptable agreement with the nominal value of $V_{Mn} = +3.33$. The axial elongation of the Mn_1O_6 octahedra in $Sr_2Al_{0.78}Mn_{1.22}O_{5.2}$ is noticeably smaller than the respective elongation in the octahedral layers of the $Sr_2Al_{1.07}Mn_{0.93}O_5$ brownmillerite (d(Mn–O)eq = 1.961 Å, $d(Mn–O)_{ap} = 2.391$ Å) [8]. This effect can be related to the higher oxidation state of the Mn cations in $Sr_2Al_{0.78}Mn_{1.22}O_{5.2}$ that results in a suppression of the Jahn-Teller distortion of the MnO_6 octahedra.

The disordered structure of the (Al, Mn) layer can be analyzed assuming that the Al1 and Mn2 atoms in these layers adopt their favorite coordination environment, namely, AlO_4 tetrahedra and MnO_6 octahedra. According to the chemical composition $Sr_2Al_{0.78}Mn_{1.22}O_{5.2}$, each $(Al_{0.78}Mn_{0.22})O_{1.2}$ layer has ~20% of octahedral sites and ~80% of tetrahedral sites. It is reasonable to assume that the AlO_4 tetrahedra share common corners and form fragments of brownmillerite-type tetrahedral chains. These fragments are interrupted by the MnO_6 octahedra that can serve as crossing points of two mutually perpendicular tetrahedral chain fragments resulting in disorder in the (Al, Mn) layer and in the average tetragonal symmetry (Fig. 4a). Note that the chain fragments can adopt one of the two mirror-related configurations ("left" (*L*) or "right" (*R*)) as it is the case in the brownmillerite structure, where the *L* and *R* chains can form a disordered or ordered arrangement resulting in modulated structures [23,24]. Two different configurations are shown with different darkness of shading in Fig. 4b. The coordination environment of the Al1 atoms is a distorted tetrahedron consisting of two O_2 atoms with $d(Al_1–O_2) = 1.751(6)$ Å and two O_3 atoms with $d(Al_1–O_3) = 1.87(3)$, 1.94(3) Å. The Mn_2 atoms are surrounded by four O_3 atoms in the equatorial plane with $d(Mn_2–O_3) = 2.019(4)$ Å. The two apical Mn_2–O_2 distances of 1.743(5) Å are too short for

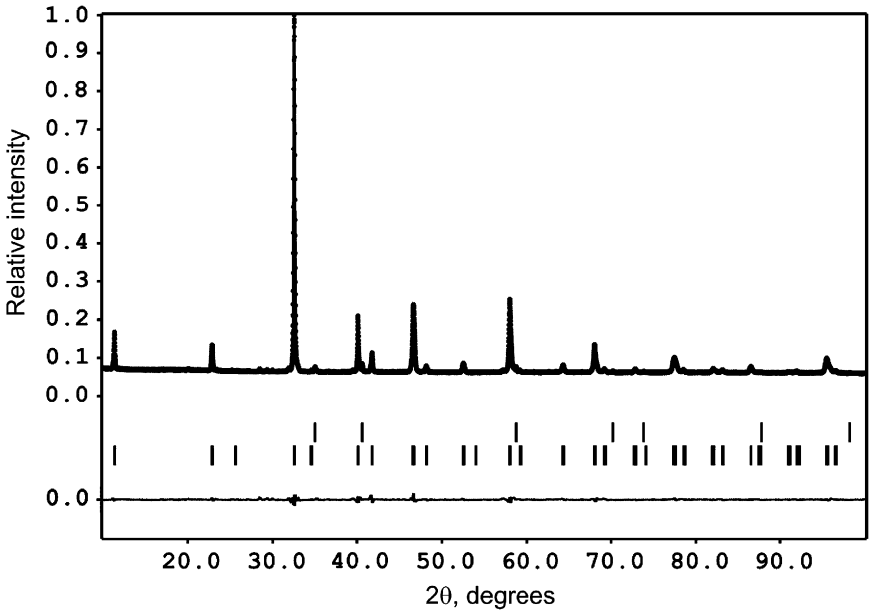

Fig. 2. Experimental, calculated and difference X-ray powder diffraction profiles for $Sr_2Al_{0.78}Mn_{1.22}O_{5.2}$.

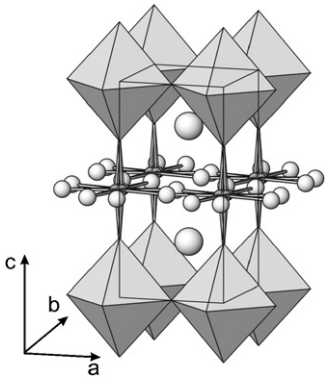

Fig. 3. The crystal structure of $Sr_2Al_{0.78}Mn_{1.22}O_{5.2}$. Mn_1 atoms are located in the octahedra, Sr atoms are shown as large spheres, the O_3 atoms are marked as medium-size spheres, Al1 and Mn2 atoms are denoted as overlapping small dark gray spheres.

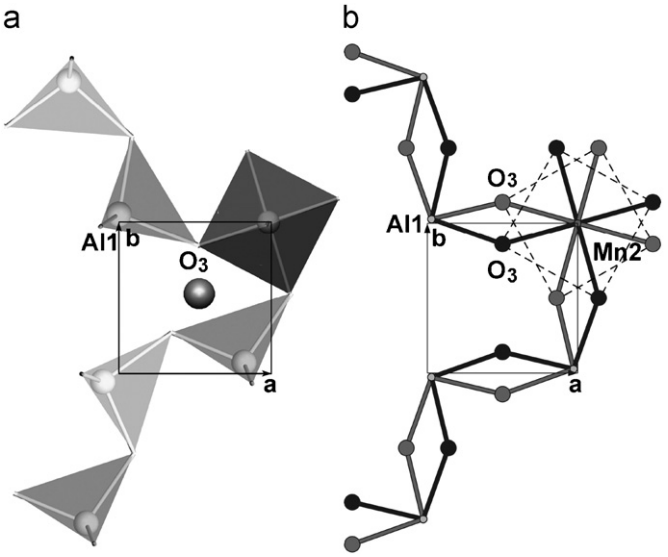

Fig. 4. The structure of the $(Al_{0.78}Mn_{0.22})O_{1.2}$ layer showing local atomic arrangement. Two mutually perpendicular fragments of Al_1–O_3 tetrahedral chains are shown crossing at the MnO_6 octahedron (a). Mirror-reflected *L* and *R* (arbitrarily) chain configurations are shown with different darkness of shading and two corresponding orientations of the MnO_6 octahedron (marked with dashed lines) (b).

the Mn cations. If the cation position in the (Al, Mn) layer is occupied by Mn, the O_2 atom bridging the Mn cations in the neighboring layers should be located close to the position $(0,0,\frac{1}{4})$ and thus provide a more appropriate Mn–O_2 distance of 1.951 Å. However, we were unable to localize the oxygen atom at this position, probably due to its low occupancy factor and the low sensitivity of XRPD to oxygen atoms. Thus, the refined *z* coordinate of the O_2 atom reflects its position in the dominating Mn_1–O_2–Al_1–O_2–Mn_1 strings along the *c* axis.

One extra fine feature which is not represented in the structure model discussed above is the further splitting of the Al_1 position due to a disordered presence of the *L* and *R* chains. This splitting would equalize the different Al_1–O_3 bond lengths, but the distance between the split positions is below the resolution of our XRPD experiment.

3.4. Electron energy loss spectroscopy

EELS spectra can be used to determine the valency of ionic species in several ways [25–28]. It was demonstrated that especially the white lines in the 3*d* transition metals are sensitive to valency changes and the position [25], total intensity or *L*3/*L*2 ratio [25,27] of this lines can be used to extract this information. Another method which was shown to give superior results is to measure the distance in energy onset between the oxygen *K* edge and the transition metal *L*23 edge of oxides as was shown for niobium oxides by Bach et al. [29]. We adopt this method here and compare the measured energy distances between the oxygen *K* edge and the manganese *L*23 edge for different reference compounds and the $Sr_2Al_{0.78}Mn_{1.22}O_{5.2}$ compound.

$Sr_2Al_{0.78}Mn_{1.22}O_{5.2}$ was measured together with references of MnO (Mn^{2+}), Mn_2O_3 (Mn^{3+}) and $CaMnO_3$ (Mn^{4+}). The reference materials were chosen to be stable towards electron beam

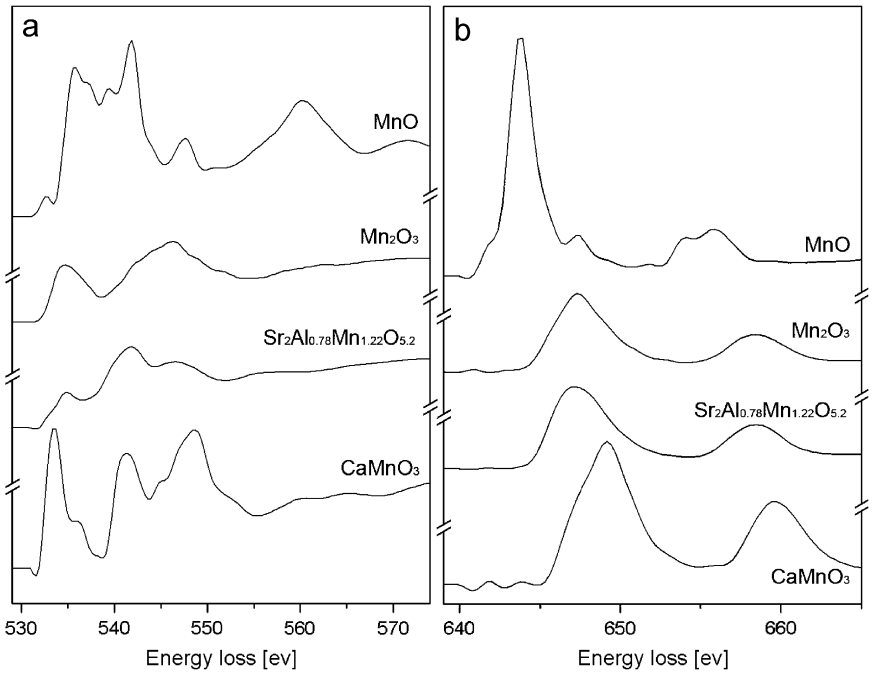

Fig. 5. The excitation edge fine structures of the oxygen *K*-edge (a) and the manganese *L*23-edge (b) from the tree reference samples and $Sr_2Al_{0.78}Mn_{1.22}O_{5.2}$ after the deconvolution of multiple scattering and background subtraction.

irradiation damage. For each reference material, 100 spectra were recorded from the same region to obtain an estimation of the effect of noise. Multiple scattering was taking into account by convoluting a model of the spectrum with a recorded low loss spectrum [19]. A power law background was used together with hydrogenic cross sections for the oxygen *K* and manganese *L*23 edge. The fine structure was taken into account by a linear interpolation between 40 points in an energy range from the edge onset till 80 eV above the edge [20]. The obtained fine structures for the reference materials (Fig. 5) are in close agreement with published data for manganese oxides [25,26,30].

The energy of the edge onset for both oxygen *K* and manganese *L*23 edges is obtained by applying a threshold of 5% of the maximum of the edge and the results are plotted in Fig. 6 together with error bars obtained from the standard deviation over the 100 spectra and taking into account that we use the average result of these 100 measurements. Linear fitting shows a relation between this energy difference (ΔE) and the manganese valence (V_{Mn}) of: $\Delta E = a + bV_{Mn}$ with $a = 104.108 \pm 0.195$ and $b = 2.238 \pm 0.063$, and R factor of 0.99961. From this relation, we can estimate the manganese valence of $Sr_2Al_{0.78}Mn_{1.22}O_{5.2}$ as $V_{Mn} = +3.29 \pm 0.03$ which is close to the nominal result of +3.33.

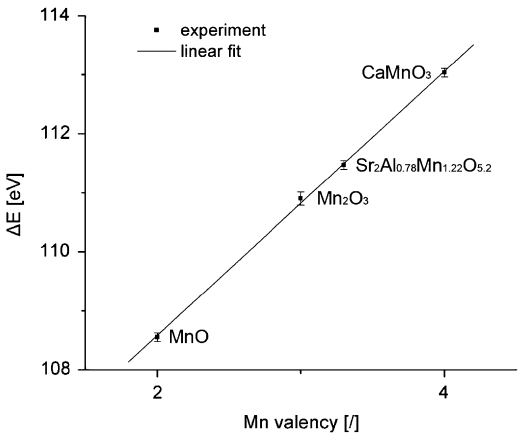

Fig. 6. Experimental results of the onset energy difference between the oxygen *K*-edge and the manganese *L*23-edge. The linear fit shows a relation between this energy difference and the manganese valence.

3.5. High-resolution TEM and HAADF-STEM imaging

High-resolution TEM imaging along the [100] zone confirms the 90° twinning as proposed based on ED patterns (Fig. 7). The Fourier transforms taken of the top-right area and the down-left area on this same HRTEM image are shown in the image as the top and bottom insets, respectively. The c^*-axis is rotated over 90° for one relative to the other. The slightly different contrast between the twin regions is due to a gradual change in specimen thickness or to strain induced at the interface. This is related to the fact that the perovskite subcell parameters are close, but not exactly equal along the *a* and *c* axes. An image calculated using the model refined from the XRPD data is included in Fig. 7 and outlined by a white border. The best agreement with the experiment was found for a focus value $f = -250$ Å and a thickness $t = 39$ Å. Under these imaging conditions, the brighter dots correspond to the cation columns. The positions of the Sr layers are indicated by black arrows, the Mn and (Al, Mn) layers can be distinguished at this specific defocus and thickness and are indicated by white arrows.

In a HAADF-STEM image, the intensity of the dots is directly related to their atomic number as $I \sim Z^n$ $(1 < n < 2)$. Due to this relation a HAADF-STEM image of the [100] zone (Fig. 8) is straightforward to interpret and gives a visualization of the alternating Mn and (Al, Mn) layers. The bright dots are the Sr columns ($Z_{Sr} = 38$). The projections of the Mn, (Al, Mn) and oxygen columns cannot be resolved on this image, but there is a clear difference in brightness at the layers separating two adjacent Sr layers. The darker layers correspond to the (Al, Mn) layers, partly occupied by light scatterers ($Z_{Al} = 13$) and depleted with oxygen atoms. The other layers appear somewhat brighter and are the Mn layers ($Z_{Mn} = 25$), as indicated in Fig. 8. The image has been sharpened by reducing the background.

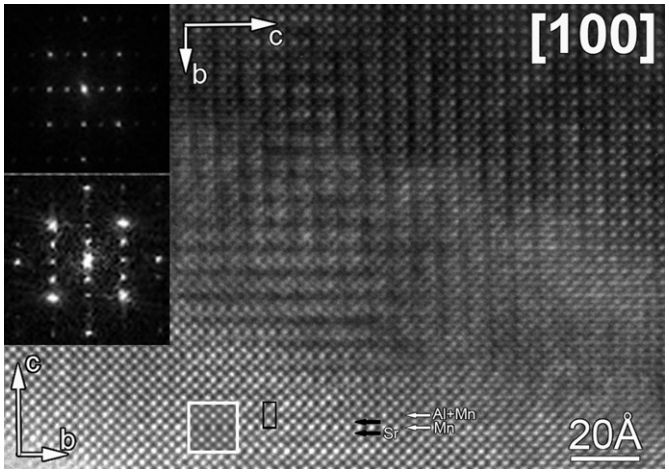

Fig. 7. HRTEM image along the [100] direction of $Sr_2Al_{0.78}Mn_{1.22}O_{5.2}$. A calculated image ($f = -250$ Å, $t = 39$ Å) is inserted and indicated by a white border, the unit cell is indicated by a black border. The Fourier transforms of different parts of the image are included in the upper left corner showing the 90° rotation twin. The different layers are indicated: Sr layers with black arrows, Mn and (Al, Mn) layers with labeled white arrows.

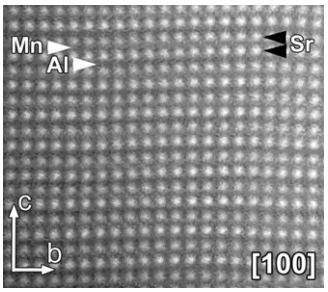

Fig. 8. HAADF-STEM image along the [100] direction of $Sr_2Al_{0.78}Mn_{1.22}O_{5.2}$. The Mn and (Al, Mn) layers are indicated with white arrows, the Sr layers with black arrows.

3.6. Magnetic properties

Magnetic susceptibility (χ) data for $Sr_2Al_{0.78}Mn_{1.22}O_{5.2}$ are shown in Fig. 9. To convert the sample magnetization into the molar susceptibility, we assumed that the sample was pure and contained the $Sr_2Al_{0.78}Mn_{1.22}O_{5.2}$ phase only. The contribution of the MnO impurity is quite weak (below 10^{-2} emu/mol for pure MnO [31], i.e., below 2×10^{-4} emu for 2% of the impurity) and can be neglected.

Above $T \approx 250$ K the susceptibility reveals a paramagnetic Curie–Weiss-like behavior. At lower temperatures there is a negative deviation from the Curie–Weiss law (see Fig. 9) indicating a tendency towards antiferromagnetic ordering. Yet in contrast to the brownmillerite $Sr_2Al_{1.07}Mn_{0.93}O_5$ [8], there are no clear anomalies that could be attributed to the onset of long-range magnetic order. Upon further decreasing the temperature, the FC susceptibility increases, shows a bend at $T_{bend} = 65$–75 K (see Fig. 9) and continues to increase down to 2 K. The ZFC curve reveals the same behavior and additionally shows a peak at 11 K. A weak kink observed in both the FC and ZFC curves at 42–45 K is likely extrinsic, since the curves do not change their slope at this point. Such a kink is usually caused by a parasitic contribution of adsorbed oxygen (β–γ transition at 43.8 K [32]), although a minor impurity of Mn_3O_4 (not visible in the XRPD data) with magnetic ordering at 42 K [33] may be another plausible reason. The magnetization curve measured at 2 K is linear (see the inset of Fig. 9) and indicates the lack of a net magnetization in $Sr_2Al_{0.78}Mn_{1.22}O_{5.2}$.

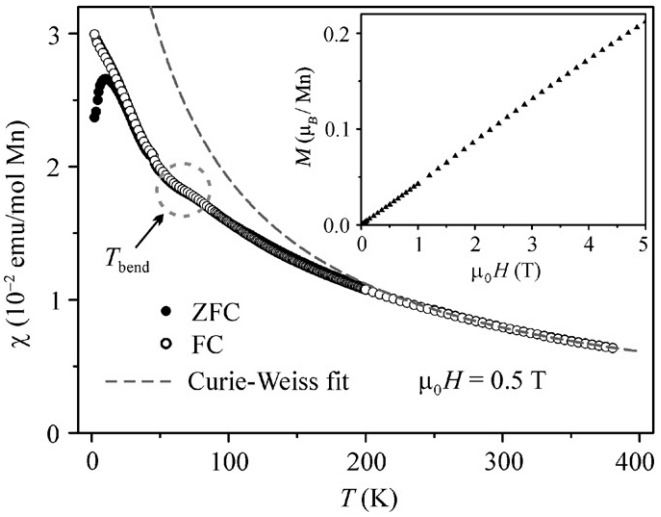

Fig. 9. Magnetic susceptibility of $Sr_2Al_{0.78}Mn_{1.22}O_{5.2}$ measured in the applied field of 0.5 T. Full and empty circles indicate the ZFC and FC curves, respectively. The dashed line shows the Curie–Weiss fit above 250 K. Large dashed circle indicates the bend at 65–75 K. The inset presents magnetization vs. field data collected at 2 K.

In general, the magnetic susceptibility data for $Sr_2Al_{0.78}Mn_{1.22}O_{5.2}$ are typical for a system with dominating antiferromagnetic interactions and a lack of long-range spin order. Such systems usually show a maximum in the χ vs. T curves due to the tendency towards antiparallel alignment of the spins at low temperature. However, in the case of $Sr_2Al_{0.78}Mn_{1.22}O_{5.2}$ the maximum is concealed by an additional paramagnetic contribution, and a bend at 65–75 K is observed instead. The paramagnetic contribution is likely caused by impurities and defects. Similar magnetic behavior with the low-temperature upturn concealing the susceptibility maximum has been reported for many low-dimensional spin systems (see e.g. [34]).

A remarkable feature of the susceptibility data is the divergence of the FC and ZFC curves below 20–25 K. Such a divergence could be an indication of spin glass behavior. Normally, the FC susceptibility of a spin glass is temperature-independent, while the ZFC susceptibility decreases with decreasing temperature. However, the addition of the paramagnetic impurity contribution results in an increase of the FC susceptibility and a peak in the ZFC curve.

The susceptibility data above 250 K can be fitted with the Curie–Weiss law $\chi = C/(T-\theta)$ resulting in $C = 2.70(1)$ emu K/mol and $\theta = -41(2)$ K. The Curie constant C corresponds to the effective moment of $4.65(1)\,\mu_B$ per Mn atom. This value is somewhat lower than the expected spin-only moment of Mn^{+3} ($S = 2$, $\mu_{eff} = 4.90\,\mu_B$). The difference is likely caused by the higher oxidation state of manganese in $Sr_2Al_{0.78}Mn_{1.22}O_{5.2}$ as evidenced by the composition and the structure refinement. Assuming a charge localization with 0.82 Mn^{+3} and 0.40 Mn^{+4} per formula unit (i.e. 67% of Mn^{+3} and 33% of Mn^{+4}), one finds the effective moment of $4.56\,\mu_B$, which is close to the experimental value. Basically, the high-effective magnetic moment implies the localization of all the d electrons in $Sr_2Al_{0.78}Mn_{1.22}O_{5.2}$. The negative Curie–Weiss temperature θ is consistent with the dominating antiferromagnetic interactions. Yet the absolute value is quite low as compared to that of related compounds (e.g., $\theta = -270$ K in Sr_2GaMnO_5 [2]). This may be explained by the presence of both ferro- and antiferromagnetic interactions in $Sr_2Al_{0.78}Mn_{1.22}O_{5.2}$, since the Curie–Weiss temperature is a

linear combination of all the exchange couplings in the system [35].

4. Discussion

A remarkable feature of the $Sr_2Al_{0.78}Mn_{1.22}O_{5.2}$ structure is the clear separation of the cations into different layers: the octahedrally coordinated Mn cations occupy separate layers alternating with the mixed (Al, Mn) layers where the Al atoms adopt a tetrahedral coordination and the Mn cations are situated within the octahedra. This ordering is coupled with an ordered alternation of oxygen-completed BO_2 layers and oxygen-depleted $BO_{1.2}$ layers, but occurs in the absence of long range anion-vacancy ordering within the anion-deficient layers. According to the interpretation of the local coordination environment of the Al and Mn atoms in the (Al, Mn) layers (as derived from the results of the Rietveld refinement), fragments of the brownmillerite structure are retained in $Sr_2Al_{0.78}Mn_{1.22}O_{5.2}$, although the infinite chains of AlO_4 tetrahedra are broken into short pieces by MnO_6 octahedra. Thus, the driving force behind the cation ordering in $Sr_2Al_{0.78}Mn_{1.22}O_{5.2}$ is essentially the same as in the $Sr_2Al_{1.07}Mn_{0.93}O_5$ brownmillerite: the difference in the coordination number and the geometry of the coordination polyhedra for Al^{+3} and $Mn^{+3+\delta}$ cations. Apparently, the origin of the layered cation order in $Sr_2Al_{0.78}Mn_{1.22}O_{5.2}$ is significantly different from that in the La_2CuSnO_6 perovskite [36], where a charge difference of two between the different *B*-cations is required for their ordering [37]. In $Sr_2Al_{0.78}Mn_{1.22}O_{5.2}$, the charge difference between the Al and Mn cations is comparable to that in the $CaRMnSnO_6$ perovskites with a disordered arrangement of the Mn^{+3} and Sn^{+4} cations [38]. The size difference of the cations also plays an important role. Ga^{+3} ($r = 0.47$ Å, CN = 4) and Mn^{+3} ($r = 0.58$ Å, CN = 6) cations have closer ionic radii than Al^{+3} ($r = 0.39$ Å, CN = 4) and Mn^{+3} cations [39]. The $SrMn_{1-x}Ga_xO_{3-x/2}$ solid solutions demonstrate a layered order of Ga^{+3} and Mn^{+3} cations only for the brownmillerite composition ($x = 0.5$), whereas for $0.1 \leqslant x \leqslant 0.3$ a disordered cubic perovskite was observed and a two-phase mixture of brownmillerite and cubic perovskite was found for $x = 0.4$ [40] instead of an intermediate layered phase, such as $Sr_2Al_{0.78}Mn_{1.22}O_{5.2}$.

Despite the structural similarity of $Sr_2Al_{0.78}Mn_{1.22}O_{5.2}$ and $Sr_2Al_{1.07}Mn_{0.93}O_5$, the magnetic properties of the two compounds are quite different. $Sr_2Al_{1.07}Mn_{0.93}O_5$ undergoes antiferromagnetic ordering at 105 K [8], while $Sr_2Al_{0.78}Mn_{1.22}O_{5.2}$ reveals a lack of long-range magnetic order. Clearly, the intermixing of the Mn and Al cations in itself does not explain this difference, since the Mn sites are partially diluted by non-magnetic Al^{+3} in both the compounds. Thus, other factors should be relevant, in particular the oxidation state of Mn and the presence of magnetic manganese cations between the ordered layers of the Mn_1O_6 octahedra.

In perovskite-like compounds, the intermediate oxidation state of Mn (between +3 and +4) often leads to spin glass behavior due to the competition of antiferromagnetic Mn–O–Mn superexchange and ferromagnetic Mn^{3+}–O–Mn^{4+} double exchange interactions. The averaged oxidation state of Mn in $Sr_2Al_{0.78}Mn_{1.22}O_{5.2}$ is +3.33, and double exchange is possible. Basically, the superexchange vs. double exchange frustration mechanism (typical for manganites) may be relevant for $Sr_2Al_{0.78}Mn_{1.22}O_{5.2}$, but there is another factor that should be even more important.

Within an intuitive approach, one would suppose that the introduction of magnetic Mn cations between the layers of Mn_1O_6 octahedra will enhance interlayer exchange coupling and increase the temperature of the magnetic ordering. However, the actual situation is completely opposite. Additional Mn cations give rise to magnetic frustration and prevent the system from reaching long-range order. In the ordered A_2BMnO_5 (B = Al, Ga) brownmillerites, the antiferromagnetic intra- and inter-layer interactions (J and J_{Al}, respectively, see Fig. 10) lead to *G*-type antiferromagnetic ordering [7,10]. Therefore, in $Sr_2Al_{0.78}Mn_{1.22}O_{5.2}$ magnetic moments on sites 1 and 2 tend to be antiparallel (see Fig. 10). If the magnetic Mn cation is located between the layers (in the Mn_2 position), the sign of the effective interlayer coupling is changed. The moments on sites 3 and 4 are coupled via two identical J_{Mn} interactions, hence these moments should be parallel (see, e.g., the example of Ca_2FeMnO_5 [41] where all the interlayer positions are filled by magnetic Fe^{+3} cations). The interactions J, J_{Al}, and J_{Mn} cannot be satisfied simultaneously, and the long-range magnetic ordering is suppressed. Note that this effect is independent of the sign of J_{Mn}.

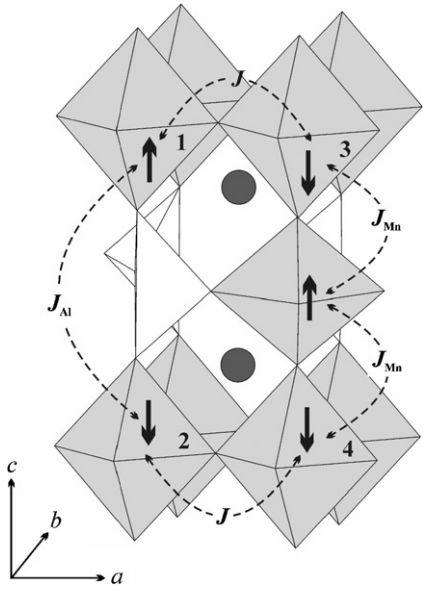

Fig. 10. Frustration of interlayer magnetic interactions in $Sr_2Al_{0.78}Mn_{1.22}O_{5.2}$. Gray polyhedra denote the MnO_6 octahedra. Thick arrows indicate parallel/antiparallel alignment of the magnetic moments and do *not* necessarily show their true directions. The antiferromagnetic interaction J_{Al} tends to antiparallel alignment of the moments on sites 1 and 2. Unlike this, the moments on sites 3 and 4 tend to be parallel, since they are coupled via two interactions J_{Mn}. The intralayer interaction J is antiferromagnetic. In this figure, antiferromagnetic J_{Mn} is assumed.

Thus, the introduction of additional Mn between the octahedral layers results in a frustration of the interlayer interactions. This mechanism naturally explains the suppression of antiferromagnetic ordering in $Sr_2Al_{0.78}Mn_{1.22}O_{5.2}$.

Acknowledgments

This work was supported by Russian Foundation of Basic Research (RFBR Grants 07-03-00664-a, 06-03-90168-a and 05-03-34812-MF-a) and, in part, by the IAP VI program of the Belgian government. The authors are grateful to Christoph Geibel for the help in magnetic susceptibility measurements and the valuable discussion. A. Ts. acknowledges the hospitality of MPI CPfS and financial support during the stay.

Appendix A. Supplementary data

Supplementary data associated with this article can be found in the online version at doi:10.1016/j.jssc.2008.11.002.

References

[1] A.M. Abakumov, M.G. Rozova, B.Ph. Pavlyuk, M.V. Lobanov, E.V. Antipov, O.I. Lebedev, G. Van Tendeloo, D.V. Sheptyakov, A.M. Balagurov, F. Bouree, J. Solid State Chem. 158 (2001) 100–111.
[2] A.M. Abakumov, M.G. Rozova, B.Ph. Pavlyuk, M.V. Lobanov, E.V. Antipov, O.I. Lebedev, G. Van Tendeloo, O.L. Ignatchik, E.A. Ovtchenkov, Yu.A. Koksharov, A.N. Vasi'ev, J. Solid State Chem. 160 (2001) 353–361.
[3] A.J. Wright, H.M. Palmer, P.A. Anderson, C. Greaves, J. Mater. Chem. 11 (2001) 1324–1326.
[4] A.J. Wright, H.M. Palmer, P.A. Anderson, C. Greaves, J. Mater. Chem. 12 (2002) 978–982.
[5] P.D. Battle, A.M. Bell, S.J. Blundell, A.I. Coldea, D.J. Gallon, F.L. Pratt, M.J. Rosseinsky, C.A. Steer, J. Solid State Chem. 167 (2002) 188–195.
[6] P.D. Battle, S.J. Blundell, P.N. Santhosh, M.J. Rosseinsky, C. Steer, J. Phys.: Condens. Matter 14 (2002) 13569–13577.
[7] V. Yu. Pomyakushin, A.M. Balagurov, T.V. Elzhov, D.V. Sheptyakov, P. Fisher, D.I. Khomskii, V. Yu. Yushankhai, A.M. Abakumov, M.G. Rozova, E.V. Antipov, M.V. Lobanov, S.J.L. Billinge, Phys. Rev. B 66 (2002) 1844121–18441213.
[8] J. Hadermann, A.M. Abakumov, H. D'Hondt, A.S. Kalyuzhnaya, M.G. Rozova, M.M. Markina, M.G. Mikheev, N. Tristan, R. Klingeler, B. Büchner, E.V. Antipov, J. Mater. Chem. 17 (2007) 692–698.
[9] A.M. Abakumov, A.S. Kalyuzhnaya, M.G. Rozova, E.V. Antipov, J. Hadermann, G. Van Tendeloo, Solid State Sci. 7 (2005) 801–811.
[10] A.M. Abakumov, M.G. Rozova, E.V. Antipov, Russ. Chem. Rev. 73 (2004) 847–860.
[11] H.M. Palmer, A. Snedden, A.J. Wright, C. Greaves, Chem. Mater. 18 (2006) 1130–1133.
[12] A.M. Abakumov, M.G. Rozova, A.M. Alekseeva, M.L. Kovba, E.V. Antipov, O.I. Lebedev, G. Van Tendeloo, Solid State Sci. 5 (2003) 871–882.
[13] A.M. Alekseeva, A.M. Abakumov, M.G. Rozova, E.V. Antipov, J. Hadermann, J. Solid State Chem. 177 (2004) 731–738.
[14] E.V. Antipov, A.M. Abakumov, A.M. Alekseeva, M.G. Rozova, J. Hadermann, O.I. Lebedev, G. Van Tendeloo, Phys. Stat. Sol. (A) 7 (2004) 1403–1409.
[15] V. Pomjakushin, D. Sheptyakov, P. Fischer, A. Balagurov, A. Abakumov, M. Alekseeva, M. Rozova, E. Antipov, Physica B 350 (2004) 23–26.
[16] V. Pomjakushin, D. Sheptyakov, P. Fischer, A. Balagurov, A. Abakumov, M. Alekseeva, M. Rozova, E. Antipov, D. Khomskii, V. Yushankhai, J. Magn. Magn. Mater. 272–276 (2004) 820–822.
[17] V. Petricek, M. Dusek, The Crystallographic Computing System JANA2000, Institute of Physics, Praha, Czech Republic, 2000.
[18] G. Bertoni, J. Verbeeck, Ultramicroscopy 108 (2008) 782–790.
[19] J. Verbeeck, S. Van Aert, Ultramicroscopy 101 (2004) 207–224.
[20] J. Verbeeck, S. Van Aert, G. Bertoni, Ultramicroscopy 106 (2006) 976–980.
[21] J. Verbeeck, G. Bertoni, Ultramicroscopy 108 (2008) 74–83.
[22] J. Hadermann, G. Van Tendeloo, A.M. Abakumov, B. Ph. Pavlyuk, M.G. Rozova, E.V. Antipov, Int. J. Inorg. Mater. 2 (2000) 493–502.
[23] S. Lambert, H. Leligny, D. Grebille, D. Pelloquin, B. Raveau, Chem. Mater. 14 (2002) 1818–1826.
[24] A.M. Abakumov, A.M. Alekseeva, M.G. Rozova, E.V. Antipov, O.I. Lebedev, G. Van Tendeloo, J. Solid State Chem. 174 (2003) 319–328.
[25] H. Kurata, C. Colliex, Phys. Rev. B 48 (1993) 2102–2108.
[26] J.H. Rask, B.A. Miner, P.R. Buseck, Ultramicroscopy 21 (1987) 321–326.
[27] T. Riedl, T. Gemming, K. Wetzig, Ultramicroscopy 106 (2006) 284–291.
[28] T. Riedl, T. Gemming, W. Gruner, J. Acker, K. Wetzig, Micron 38 (2007) 224–230.
[29] D. Bach, H. Stormer, R. Schneider, D. Gerthsen, J. Verbeeck, Microscopy Microanal. 12 (2006) 416–423.
[30] J. Jimenez-Mier, D.L. Ederer, T. Schuler, Radiat. Phys. Chem. 75 (2006) 1666–1669.
[31] D. Bloch, J.-L. Feron, R. Georges, I.S. Jacobs, J. Appl. Phys. 38 (1967) 1474–1475.
[32] Yu.A. Freiman, H.J. Jodl, Phys. Rep. 401 (2004) 1–228.
[33] K. Dwight, N. Menyuk, Phys. Rev. 119 (1960) 1470–1479.
[34] E.E. Kaul, H. Rosner, V. Yushankhai, J. Sichelschmidt, R.V. Shpanchenko, C. Geibel, Phys. Rev. B 67 (2003) 1744171–17441710.
[35] N.W. Ashcroft, N.D. Mermin, Solid State Physics, Harcourt College Publishers, 1976 (Chapter 33).
[36] M.T. Anderson, K.R. Poeppelmeier, Chem. Mater. 3 (1991) 476–482.
[37] M.T. Anderson, K.B. Greenwood, G.A. Taylor, K.R. Poeppelmeier, Prog. Solid State Chem. 22 (1993) 197–233.
[38] A.M. Abakumov, M.D. Rossell, S.A. Seryakov, M.G. Rozova, M.M. Markina, G. Van Tendeloo, E.V. Antipov, J. Mater. Chem. 15 (2005) 4899–4905.
[39] R.D. Shannon, C.T. Prewitt, Acta Cryst. B 25 (1969) 925–945.
[40] E.N. Caspi, M. Avdeev, S. Short, J.D. Jorgensen, B. Dabrowski, O. Chmaissem, J. Mais, S. Kolesnik, J. Solid State Chem. 177 (2004) 1456–1470.
[41] A.I. Rykov, K. Nomura, Y. Ueda, A.N. Vasiliev, J. Magn. Magn. Mater. 320 (2008) 950–956.